IEEE Access
Multidisciplinary | Rapid Review | Open Access Journal

Received August 24, 2017, accepted September 18, 2017, date of publication September 20, 2017,
date of current version November 14, 2017.

Digital Object Identifier 10.1109/ACCESS.2017.2754985

Antenna Diagnostics and Characterization Using Unmanned Aerial Vehicles

MARÍA GARCÍA-FERNÁNDEZ[1], (Student Member, IEEE), YURI ÁLVAREZ LÓPEZ[1], (Senior Member, IEEE), ANA ARBOLEYA[2], BORJA GONZÁLEZ-VALDÉS[3], (Member, IEEE), YOLANDA RODRÍGUEZ-VAQUEIRO[3], (Student Member, IEEE), MARÍA ELENA DE COS GÓMEZ[1], (Member, IEEE), AND FERNANDO LAS-HERAS ANDRÉS[1], (Senior Member, IEEE)

[1]Área de Teoría de la Señal y Comunicaciones, Universidad de Oviedo, 33203 Gijón (Asturias), Spain
[2]Polytech' Nice-Sophia, Dpt Electronique, 06410 Biot, France
[3]AtlantTIC Research Center Campus Lagoas-Marcosende. 36310 Vigo, Pontevedra

Corresponding author: Yuri Álvarez López (alvarezyuri@uniovi.es)

This work was supported in part by the Ministerio de Economía, Industria y Competitividad, Gobierno de España of Spain/FEDER, under Project TEC2014-54005-P (MIRIIEM), Project TEC2015-73908-JIN, Project TEC2014-55290-JIN (PORTEMVISION), and Grant FPU15/06341, in part by the Principado de Asturias, through the Plan de Ciencia, Tecnología e Innovación 2013–2017, under Project GRUPIN14-114, and in part by the Galician Regional Government and the Plan I2C (2011–2015) under Project CN2012/279 and Project CN2012/260 (AtlantTIC).

ABSTRACT This paper presents a compact, low-cost unmanned aerial system for antenna measurement. The proposed system overcomes existing limitations in terms of unmanned aerial vehicle positioning and data geo-referring accuracy using a real-time kinematic positioning system to achieve centimeter-level accuracy. Amplitude-only measurements acquired using a low-cost power sensor are processed by means of the phaseless sources reconstruction method. This is an iterative phase retrieval technique that allows recovering an equivalent currents distribution, which characterizes the antenna under test (AUT). From these equivalent currents, near-field to far-field transformation is applied to calculate the AUT radiation pattern. This contribution also analyzes probe antenna characterization and the impact of positioning and geo-referring accuracy on the radiation pattern. Two application examples of antenna measurement at S- and C-bands using the implemented system are presented.

INDEX TERMS Unmanned aerial vehicles (UAVs), antenna measurement, antenna diagnostics, real time kinematic (RTK), phaseless measurements, near-field to far-field transformation (NF-FF), sources reconstruction method (SRM).

I. INTRODUCTION

In the last years Unmanned Aerial Vehicles (UAVs) have experienced a great cost reduction while improving technical capabilities such as avionics and propulsion systems [1], batteries capacity, obstacle avoidance methods [2], multiband communications [3], and sensor integration. These achievements have fostered the introduction of UAVs in a wide field of applications such as archaeology [4], environmental monitoring [5], civil engineering [6], and assistance in natural disasters [7].

In the field of electromagnetic emissions and antenna measurement, UAVs have enabled the possibility of performing in-situ evaluation of radiating systems [8], [9]. This kind of measurements, although less accurate than those performed in anechoic chambers or outdoor ranges, allow the evaluation of the antenna radiation pattern in realistic conditions, as well as assessing the influence of the environment in the radiation pattern (e.g. distortion due to multipath contributions in ground, surrounding structures, etc.).

Current UAV-based antenna measurement systems are mostly based on an antenna connected to a power detector or a spectrum analyzer onboard the UAV, which transmits the measured data and UAV position to a ground station. A waypoint path defined around the Antenna Under Test (AUT) is pre-defined prior operation [8], [10]. In some implementations, the UAV is equipped with a continuous wave transmitter, being the AUT the receiver [11].

UAV-based antenna measurement systems have been introduced for practical applications and projects such as testing the antennas for the Square Kilometer Array (SKA)

project [12], assessing the integrity of radionavigation signals (VHF omni-directional range, VOR) [13], and characterizing cellular and multimode networks [8]. These results prove the accuracy and cost effectiveness of UAV-based systems over traditional land-based solutions or manned aircraft based surveys for in-situ antenna characterization.

The aforementioned UAV-based antenna measurement systems are based on direct measurement of the radiation pattern, with the UAV acquiring data in the far field (FF) region of the antenna. For low frequencies or electrically large antennas, the far field region can be hundreds of meters from the AUT. This fact has two main advantages: i) positioning errors are less critical as acquisition points can be separated tens of meters, and ii) Near-Field to Far-Field (NF-FF) transformation is not required to obtain the AUT radiation pattern. However, there are some drawbacks: i) longer flight path for full pattern measurement, which might require several flights due to UAV flight autonomy, ii) flight restrictions that may limit the scan zone (e.g. flying over crowded areas, restricted zones, beyond visual line of sight). These constraints may limit the practical implementation of the method.

To overcome these limitations, and thanks to the improvements in UAV positioning and data geo-referring accuracy, Near Field (NF) measurements have been proposed [14], [15] describe a NF antenna measurement technique using airborne NF-probes onboard UAVs, and a laser tracking system for accurate positioning, whereas in [16] an analysis of different scanning strategies (definition of acquisition grids using waypoints) is presented.

The concept of performing antenna diagnostics from NF measurements is already mentioned in [15] and [16]. Yet, Near-Field to Near-Field (NF-NF) transformation to recover the field in the vicinity of the AUT (e.g. aperture fields) enables antenna diagnostics capabilities, which is of great interest in order to detect malfunctioning elements or distortions in the antenna structure [17]. When dealing with complex AUT geometries, the use of an equivalent current distribution reconstructed from NF measurements on a surface fitting the AUT geometry has been proved to be a successful methodology for antenna diagnostics [18]–[20]. Besides, once the equivalent currents are reconstructed, NF-FF can be applied to obtain the AUT radiation pattern.

In order to keep the cost and the complexity of the UAV-based antenna measurement system low, amplitude-only acquisition is preferred, avoiding the need of coherent receivers for phase measurements. Thus, in order to perform NF-NF and NF-FF transformations, phase retrieval methods [21] have to be considered. In addition to this, aiming to keep the hardware complexity onboard the UAV as low as possible, iterative phase retrieval techniques based on equivalent currents [22] are used instead of indirect holographic techniques [23].

This contribution presents a UAV-based system for antenna diagnostics and characterization (*Unmanned Aerial System for Antenna Measurement*, UASAM) which tries to overcome some of the limitations in current state-of-the-art systems.

A. HIGHLIGHTS

The main advantages and novelties of the system presented in this contribution (UASAM) with respect to similar systems are:

i) Use of a compact, low-cost UAV, thanks to the fact that the payload is reduced to a low profile antenna and a power detector.

ii) Centimeter-level accuracy data geo-referring achieved by means of a Real Time Kinematic (RTK) system, which is a differential Global Navigation Satellite System (GNSS) that makes use of the GNSS carrier phase [24]. A laser altimeter is integrated to improve accuracy in height.

iii) Capability of AUT diagnostics and characterization from NF phaseless measurements, thanks to the use of the phaseless Sources Reconstruction Method (pSRM) that can handle arbitrary-geometry NF grids [23] (details in Section III).

iv) Low sensitivity to UAV positioning (as it will be explained in Section IV), which can be of interest in windy operating conditions.

An overview of the UASAM features can be watched in the video accompanying this contribution.

II. DESCRIPTION OF THE SYSTEM

A. HARDWARE DESCRIPTION

The developed UASAM prototype is composed by the following devices and subsystems, depicted in Fig. 1:

i) A UAV with a power detector, a probe antenna, and a RTK beacon onboard.

ii) A second RTK beacon acting as a base station for the RTK system, placed at a fixed position.

iii) A ground station (typically a laptop) that receives amplitude-only measurements and positioning information from the UAV (RTK coordinates and laser altimeter altitude readings), and processes this information to geo-reference amplitude-only measurements with cm-level accuracy.

Similarly to [15], UAV flight path around the AUT is defined using waypoints, so different kinds of grids (cylindrical, planar) can be created depending on the AUT characteristics. The use of waypoints also allows repeating the measurement procedure if needed.

The communication system between UAV, RTK beacons, and the ground station is implemented using a Wireless Local Area Network (WLAN), operating in the 2.4-2.5 GHz and 5.7-5.8 GHz frequency bands. UAV control is based on 433 MHz radio transmitter and receiver to avoid interferences with the working frequency band.

Fig. 2 shows a picture of the UAV with the RTK and the probe printed monopole antenna onboard.

The UAV frame is composed by the F550 model of DJI [25], with a total 2400 g payload capacity. The UAV is controlled with a Navio2 board [26] attached to a Raspberry Pi running ArduCopter [27].

A printed monopole antenna is selected as a probe. The choice of this kind of antenna and its characterization is

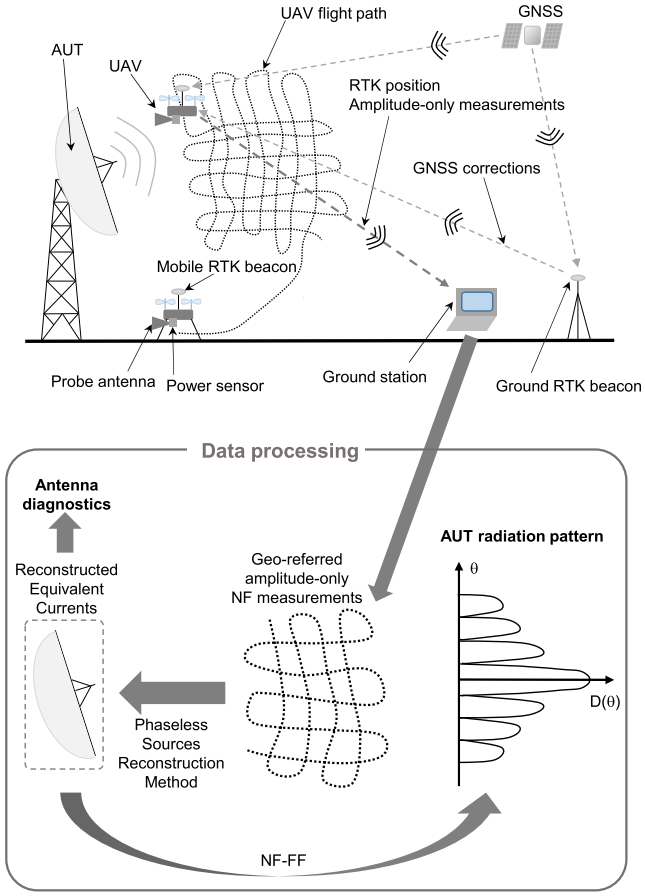

FIGURE 1. Overview of the unmanned aerial system for antenna Measurement (UASAM).

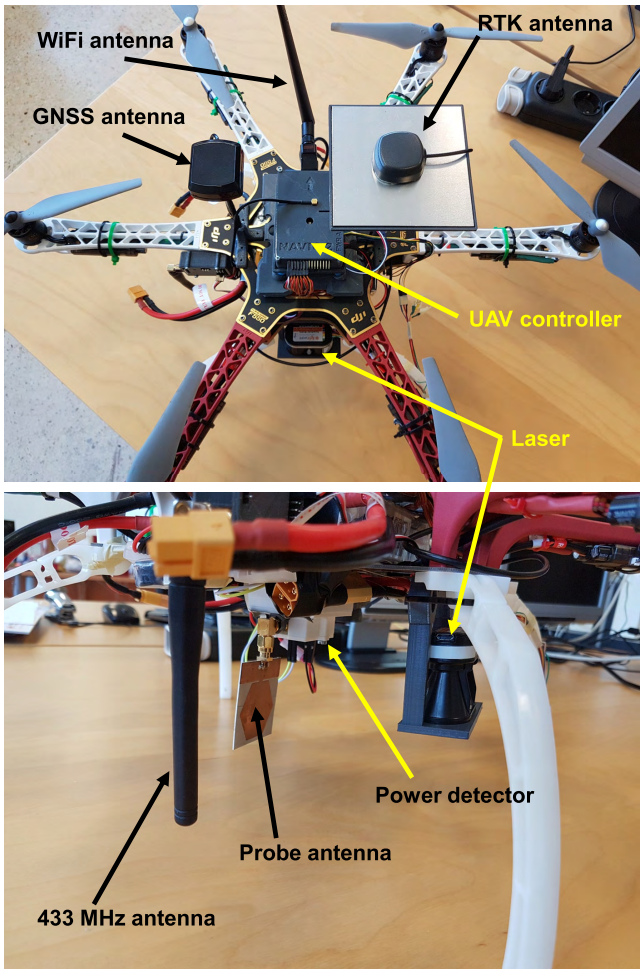

FIGURE 2. UAV with the RTK and the probe printed monopole antenna onboard.

explained in Section III. The onboard probe antenna is connected to a compact, low-cost power sensor based on the AD8318 chip [28], which has a dynamic range of 50 dB. The analog output is digitalized and passed to the Raspberry Pi, then sent to the ground station together with the RTK positioning information.

The RTK system consists of two units based on the *u-blox* NEO-M8T chip [29] acting as RTK beacons. One is designed as the mobile RTK beacon, placed onboard the UAV. As depicted in Fig. 2, the RTK antenna is placed over a ground plane in a pole at the top of the UAV. The RTK beacon working as base station is placed on a tripod at a fixed, known position. This base station beacon forwards the corrections that must be applied to the GNSS signal to the RTK beacon placed in the UAV (as depicted in Fig. 1). The latter applies these corrections reducing the position uncertainty down to cm-level.

A compact laser altimeter [30] is also mounted at the bottom of the UAV frame to improve the accuracy of height positioning. The flight controller combines the positioning and attitude information data provided by the positioning systems (RTK, laser altimeter, inertial sensors, standard GNSS and barometer) to obtain the geodetic coordinates (Latitude, Longitude and Height), which are sent to the ground station together with a time stamp.

The ground station runs the algorithms that process the geo-referred amplitude-only field measurements to calculate the antenna radiation pattern and to obtain antenna diagnostics information.

B. PHASELESS SOURCES RECONSTRUCTION METHOD

One of the drawbacks of using power detectors for antenna measurement is that phase information cannot be directly measured, thus requiring phase retrieval methods [21]–[23]. The UASAM makes use of the phaseless Sources Reconstruction Method (pSRM), an iterative phase retrieval technique where an equivalent electric and magnetic currents distribution is recovered on a surface enclosing the AUT [22]. Iterative phase retrieval techniques require the measurement of the NF on two or more acquisition surfaces, as the spatial variation of the field distribution with distance in the AUT NF region contains sufficient information to allow for phase recovery [22].

As a simplified scheme but without losing generality, an infinite plane can be considered as the enclosing surface (reconstruction domain); then, the Second Equivalence Principle [31] can be established to reconstruct the magnetic

equivalent currents that radiate the same field as the AUT outside the reconstruction domain. As explained in [22], the enclosing surface can be truncated in some cases to a plane placed on the AUT aperture.

The reconstructed equivalent currents provide antenna diagnostics and, by means of NF-FF transformation, the AUT radiation pattern can also be calculated.

The flowchart of the pSRM is shown in Fig. 3. The inputs are the measured amplitude of the radiated field, geo-referred with cm-level accuracy thanks to the RTK system, and an initial guess for the equivalent currents (e.g. a uniform distribution on the area covering the antenna aperture, $I_{\text{eq}} = 1$, and $I_{\text{eq}} = 0$ elsewhere).

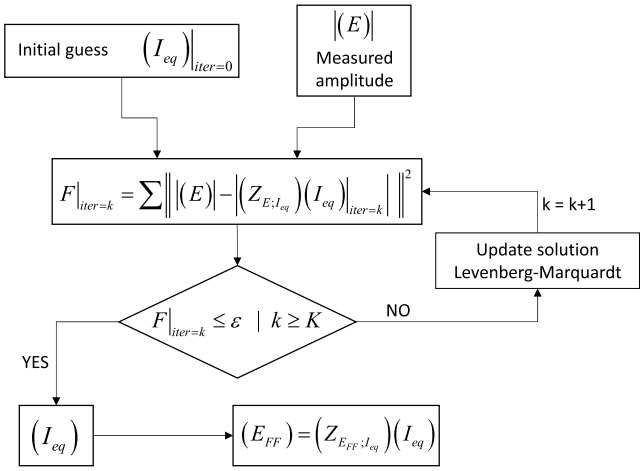

FIGURE 3. Flowchart of the pSRM.

Then, a non-linear cost function relating the measured amplitude and the amplitude of the field radiated by the equivalent currents is minimized. For this purpose, non-linear optimization techniques, such as Newton-Raphson and Levenberg-Marquardt, have been considered. The iterative algorithm stops if the cost function value is smaller than a certain threshold (ε), or if a maximum number of iterations (K) is reached. Finally, from the equivalent currents, the field at any point of the space as well as the AUT radiation pattern can be evaluated.

An important feature of the SRM [19] (and also the phaseless version pSRM) is the capability of handling arbitrary-geometry field acquisition and equivalent currents reconstruction domains, provided that they are properly sampled, i.e. adjacent points spaced $\Delta R \le \lambda/2$ in the case of amplitude and phase measurements, and $\Delta R \le \lambda/4$ for amplitude-only acquisitions [32].

To reduce the calculation time of the pSRM, the algorithm has been coded using Graphics Processing Units (GPU) [33].

III. PROBE ANTENNA CHARACTERIZATION

A key component of the UASAM is the probe antenna. During the design stage several options already used in related works, such as dipole antennas [11], log-periodic antenna arrays [10], biconical probes, or horn antennas [14], were considered. However, the use of directive antennas would require probe correction techniques. Besides, UAV attitude uncertainties will have a higher impact in NF measurements when considering directive probes due to AUT – probe orientation misalignments. For this reason, low-directive antennas have been widely considered as probes for UAV-based antenna measurement systems, and so for the UASAM.

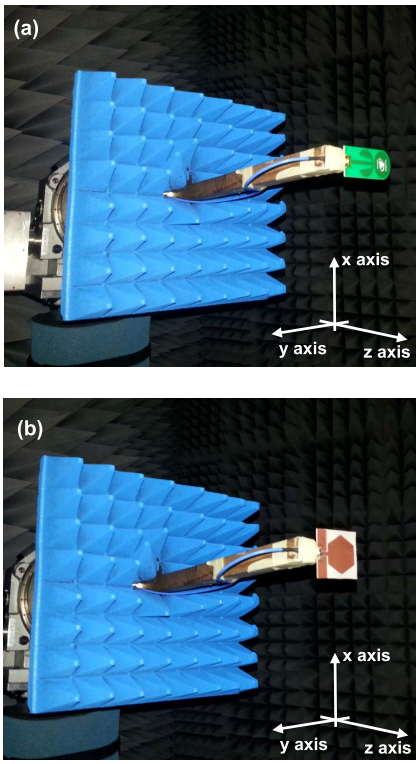

FIGURE 4. Printed monopole antennas considered as probes, tested at the spherical range in anechoic chamber of the University of Oviedo. (a) Commercial printed monopole antenna. (b) Customized hexagon-shaped printed monopole antenna.

Besides directivity, there are other parameters, such as working frequency band, bandwidth, weight, size, and polarization purity that must be taken into account for probe antenna selection. In this contribution, S and C bands will be considered.

Printed monopole antennas fulfill the requirements of low directivity, low weight and compact size. Two printed monopole antennas, shown in Fig. 4, are considered. The first one is a commercial antenna [34] working in the 4 to 7 GHz band (S_{11} depicted in Fig. 5), and the second one is a customized hexagon-shaped printed monopole antenna [35], working in the 2.5 to 5 GHz frequency band (2.6 to 4.7 GHz if a -17 dB S_{11} threshold is considered, Fig. 5).

Radiation patterns of such probes have been measured at the spherical range in anechoic chamber of the University of Oviedo at the frequency of 4.65 GHz. From Fig. 6 it can be concluded that the commercial monopole antenna exhibits better symmetry with respect to the H plane (XZ plane in Fig. 6). In the case of the customized hexagon-shaped

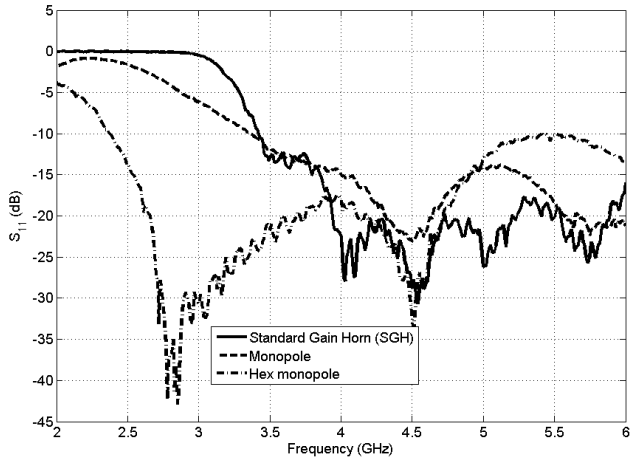

FIGURE 5. Comparison of the S_{11} (amplitude, dB) of a Standard Gain Horn (SGH) (solid line), a commercial printed monopole antenna (dashed line), and a customized hexagon-shaped printed monopole antenna (dash-dotted line).

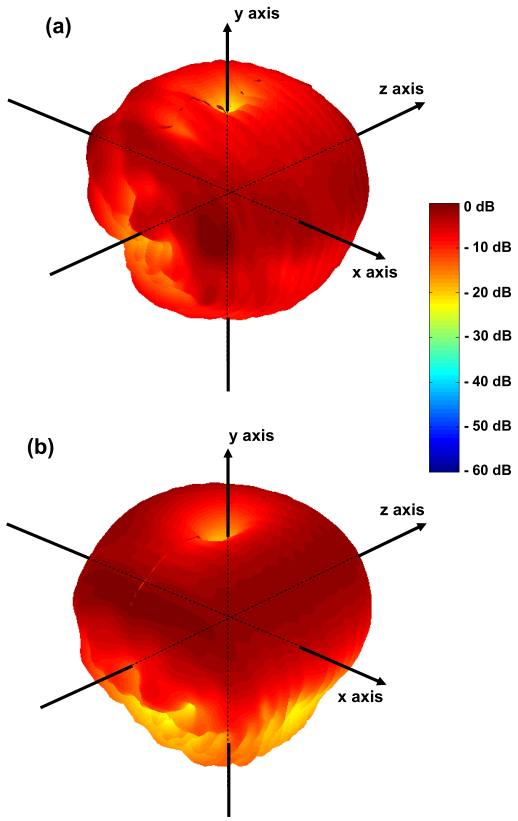

FIGURE 6. Normalized radiation pattern of the (a) commercial printed monopole antenna [34] and (b) customized hexagon-shaped printed monopole antenna [35].

printed monopole antenna, it has better rotation symmetry around y axis than the commercial monopole antenna.

Next, the accuracy of the measurements when considering these monopoles as probes has been benchmarked against a Standard Gain Horn (SGH) antenna at 4.65 GHz. For this test, a second hexagon-shaped printed monopole antenna has

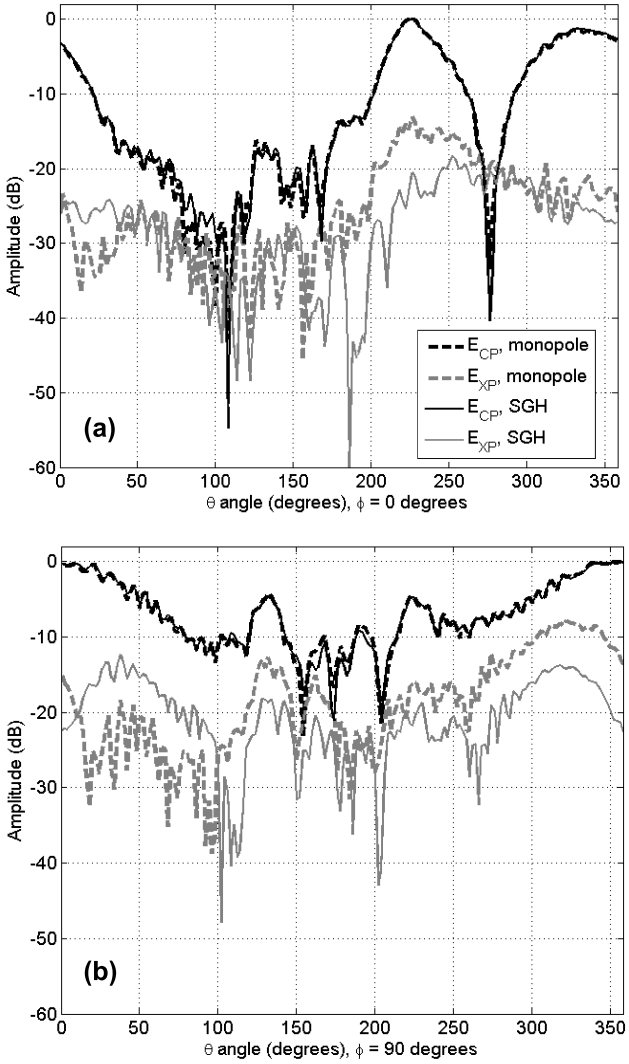

FIGURE 7. Customized hexagon-shaped printed monopole antenna radiation pattern. Main cuts (normalized amplitude, in dB). Comparison of measurement results using a SGH and the commercial printed monopole antenna as probes.

been chosen as the AUT. Measurement results at the spherical range in anechoic chamber for the commercial printed monopole antenna are depicted in Fig. 7. It can be noticed the agreement in the copolar component for both probes. However, in the case of the crosspolar there are some discrepancies. This is due to the fact that the crosspolar level of the printed monopole antenna is 15-20 dB higher than the SGH.

IV. ACCURACY ANALYSIS

One of the most critical parameters concerning UAV-based NF measurements is UAV positioning. Inertial navigation systems, GNSS uncertainties, and weather conditions introduce deviations in the flight path of the UAV with respect to the pre-defined one.

UAV positioning error is defined as the distance between the targeted and real flight path, whereas geo-referring error is the distance between the true UAV position and the

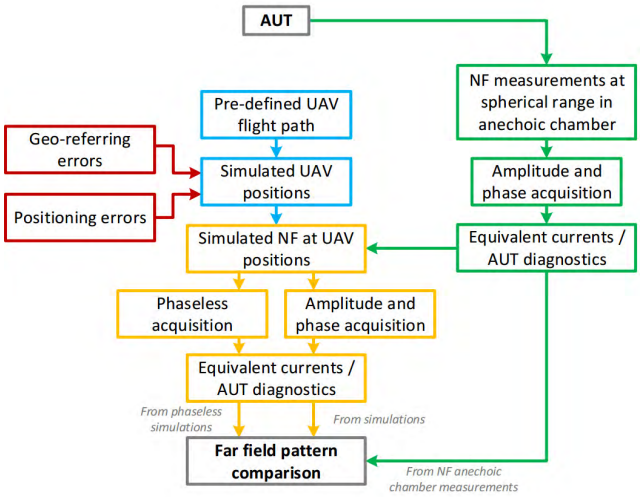

FIGURE 8. Flowchart of the procedure to evaluate the impact of positioning and geo-referring errors in the far field pattern.

UAV position estimated by the RTK, laser altimeter, and inertial sensors.

In the case of FF measurements, where the separation between waypoints can be tens of meters, positioning errors with current UAV positioning and navigation systems can be around 1 m, having little impact in the measurements [8]–[12].

In the case of NF measurements, the use of NF-NF techniques capable of handling arbitrary-geometry acquisition domains [18], [19] overcomes the requirement of accurate positioning provided that the positions where data is acquired are accurately geo-referred. To address this problem, [15] proposes the use of a laser-tracker system, that provides mm-level accuracy (enabling measurements up to 40 GHz) but at the expense of increasing the complexity of the system and its cost.

UASAM uses a RTK module and a laser altimeter for positioning and data geo-referring with cm-level accuracy. That limits the upper working frequency to approximately 5-6 GHz ($\lambda/4 = 1.5$ - 1.9 cm), but still covers the working frequency band of a wide variety of wireless communications systems (e.g. radio and television broadcasting, and/or mobile networks, radionavigation systems).

An analysis of the impact of positioning and geo-referring errors is conducted next, following the procedure depicted in Fig. 8. For this purpose, an AUT consisting of a linear array of two horn antennas working at 4.65 GHz (for further details please refer to Section V.B) has been measured at the spherical range in anechoic chamber. Then, an equivalent currents model has been calculated to have an electromagnetic equivalent model of the AUT which allows the evaluation of the field radiated by the AUT at the positions of interest [22].

Two cylindrical acquisition domains of radius $R = 3$ m and $R = 4$ m and height $h = 2$ m have been defined. The coordinates of the cylindrical acquisition domain are the targeted UAV flight path. The targeted flight path is compared

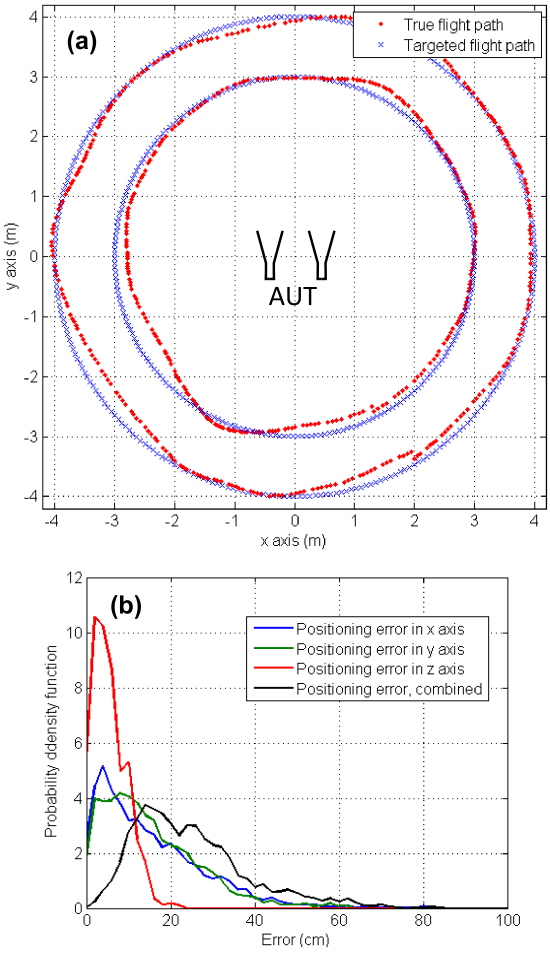

FIGURE 9. (a) Targeted and true flight paths in the XY plane. (b) Probability density function of the positioning errors in x, y, z axes, and combined.

against the true UAV flight path (Fig. 9) in order to quantify the positioning errors. The probability density function of the error (Fig. 9 (b)) shows that the positioning error in x and y axes is around 15-30 cm, whereas in z it is reduced to less than 10 cm.

The geo-referring uncertainty of the RTK system has been measured by placing the UAV at a fixed location, then recording RTK geolocation data for ten minutes. The same experiment has been done in a different day, placing the drone in another position. In the horizontal plane (x, y axes), RTK geo-referring standard deviation is approximately $\sigma_{x,y} =$ 1-1.5 cm. However, in height (z axis), RTK geo-referring standard deviation increases up to $\sigma_z =$ 3-4 cm. This uncertainty is reduced to $\sigma_z =$ 1-2 cm thanks to the use of the laser altimeter [30].

In order to evaluate the impact of geo-referring errors in the radiation pattern, random errors following a normal probability density function N(0, σ) are introduced in the true UAV flight path coordinates.

From the equivalent currents model of the AUT, NF has been calculated at: i) targeted UAV positions, ii) true UAV positions with no geo-referring error, and iii) true

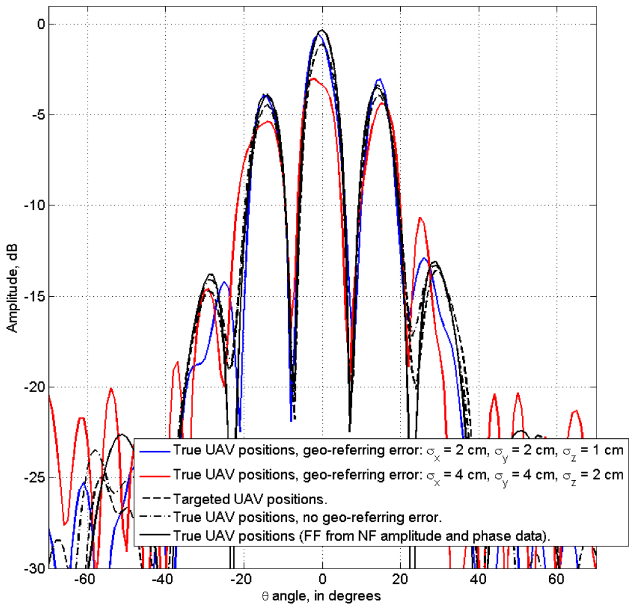

FIGURE 10. Impact of positioning and geo-referring errors in the far field pattern (H plane, $\varphi = 0°$) when considering amplitude-only NF data. FF pattern form NF amplitude and phase data (black line) is depicted as a reference.

UAV positions with geo-referring error. Next, the pSRM is applied to calculate the AUT FF pattern from the amplitude of the calculated NF, considering positioning and geo-referring errors.

Results depicted in Fig. 10 show that positioning errors (with no geo-referring error) have little impact in the radiation pattern (less than 1 dB difference). However, even when considering the low measured geo-referring uncertainty of the UASAM ($\sigma_{x,y} = 2$ cm, $\sigma_z = 1$ cm), differences in the sidelobe levels can be noticed. Increasing the geo-referring uncertainty to $\sigma_{x,y} = 4$ cm, $\sigma_z = 2$ cm increases these differences.

To sum up, the capability of the pSRM to handle arbitrary-geometry acquisition domains minimizes the impact of UAV positioning errors in the calculation of the FF pattern from amplitude-only NF measurements. However, the true coordinates of the measurement positions must be precisely known.

V. VALIDATION

Aiming to test the UASAM upper frequency limits for antenna measurement, two application examples at S and C bands respectively are presented. Tests have been conducted at the airfield authorized by the Spanish Agency of Air Safety (AESA) located at the Technical School of Engineering of Gijón (coordinates 43.521698, −5.623983).

Antenna diagnostics and FF pattern results have been benchmarked against measurements at a spherical range in anechoic chamber. Measurement uncertainties have been assessed by comparing the measured NF with the field radiated by an equivalent currents model of the AUT at the UAV positions, as depicted in the flowchart of Fig. 11.

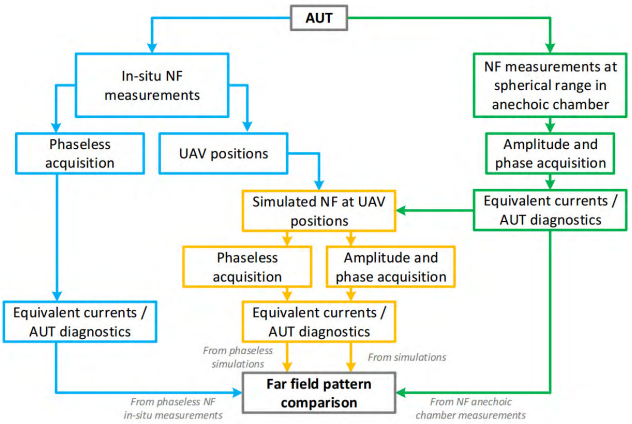

FIGURE 11. Flowchart of the procedure for antenna diagnostics and radiation pattern evaluation from phaseless NF measurements (boxes and arrows in blue). Comparison with simulated NF (boxes and arrows in yellow) and reference measurements (boxes and arrows in green).

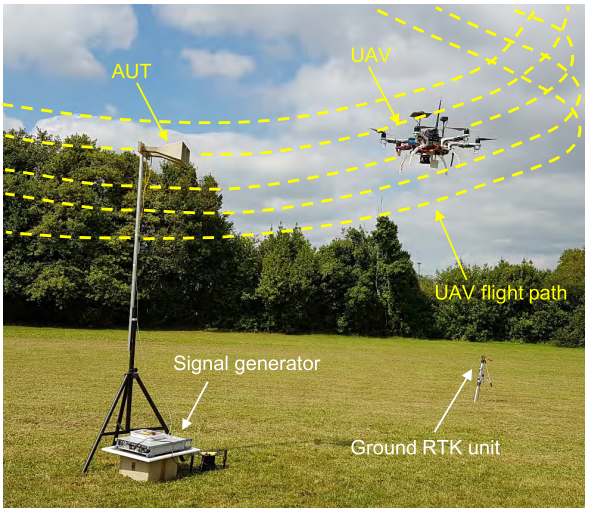

FIGURE 12. Picture of the UASAM measurement setup. AUT: array of two horn antennas at 2950 MHz.

A. S-BAND HORN ANTENNA ARRAY

The first AUT consists of an array of two horn antennas working in the 2.5 – 4 GHz frequency band, measured at the frequency of 2950 MHz using the customized hexagon-shaped printed monopole antenna. The separation between the two horn antennas is 2.6 λ (26 cm), resulting in a radiation pattern with several grating lobes.

The power of the signal generator is +10 dBm. The output is connected to a power divider to feed both horn antennas. The AUT is placed in the center of the airfield, at the top of a 3 m height pole (see Fig. 12). The ground RTK unit is deployed around 10 m away from the AUT. The ground station (a laptop) is set at one of the edges of the airfield. For this AUT, the FF region starts at $R_{FF} = 2D^2/\lambda = 4.9$ m [32] (with $D = 0.5$ m, the AUT size).

Different acquisition domains can be considered (planar, cylindrical, spherical). The UAV is capable of flying around the vertical axis of the AUT while keeping the orientation

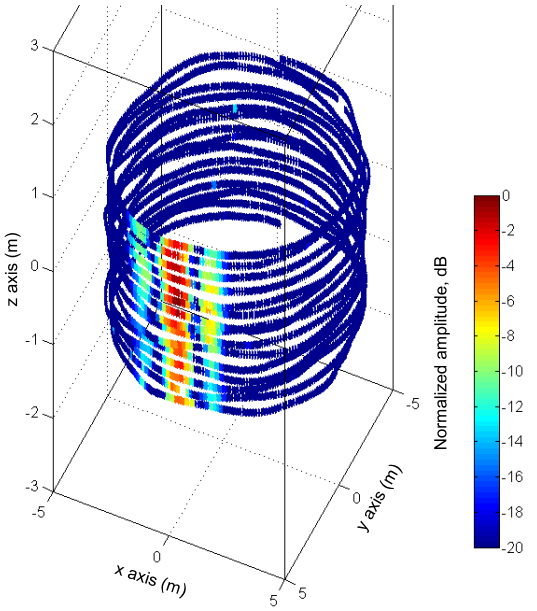

FIGURE 13. Measured amplitude of the NF radiated by the AUT at the UAV flight path positions. Targeted flight path: cylindrical domain of radius $R = 4.5$ m. $f = 2950$ MHz. Axes centered at the AUT position.

towards that axis. Thus, a cylindrical acquisition path has been found to be the NF measurement domain most suitable for this case, as it only introduces truncation error in the vertical axis. Two cylinders of R = 3 m and R = 4.5 m, and height ranging from 2 m to 4 m have been considered, sampling every 15 cm in height.

UASAM deployment and setup time took around 15 min for this example. Measurement time for each cylindrical surface was approximately 10 min (R = 3 m) and 15 min (R = 4.5 m), with the UAV moving at 1.2 m/s. Measurements are taken every 25 ms, so the spacing between two consecutive positions in the horizontal plane is 3 cm (0.3 λ). An average of 750 samples per ring (z = constant) of the cylindrical domains are taken. It results, for this example, in around 22500 NF samples.

Measurements were geo-referred using the information provided by the different sensors (RTK, laser altimeter, inertial sensors). As observed in Fig. 13, the main lobe and the sidelobes (actually, grating lobes) can be noticed.

For validation purposes, the AUT has been measured at the spherical range in anechoic chamber, then applying the SRM to obtain an equivalent model of the AUT to evaluate the NF at the UAV measurement positions. A comparison between the amplitude of the measured NF and the NF radiated by the electromagnetic equivalent model of the AUT at UAV positions is depicted in Fig. 14 (XZ plane projection) and Fig. 15 (H plane). Differences are mainly due to orientation misalignment between the AUT and the probe antenna (wind gusts and positioning errors influence the UAV steering towards the AUT).

Geo-referred NF measurements are post-processed by the pSRM. Equivalent magnetic currents (that is, aperture

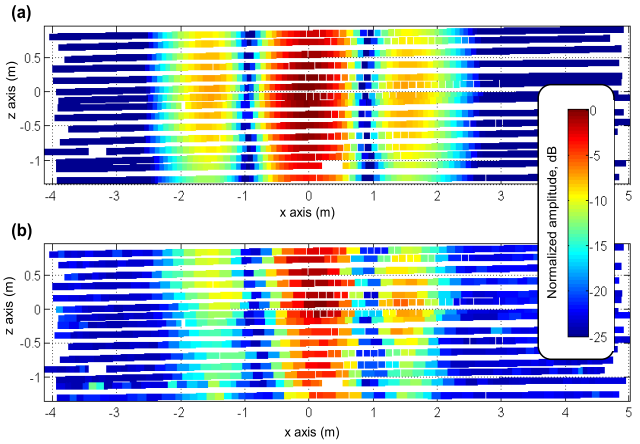

FIGURE 14. NF amplitude at UAV positions, $f = 2950$ MHz (targeted flight path: R = 4.5 m radius cylinder). (a) Simulated from AUT equivalent currents model. (b) UASAM measurements.

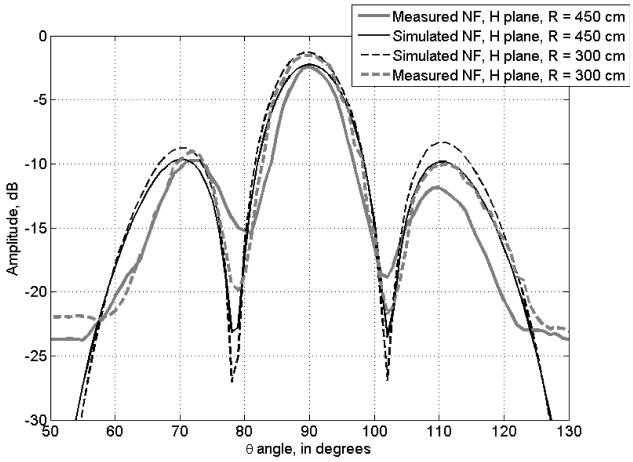

FIGURE 15. NF amplitude, H plane. $f = 2950$ MHz. Comparison between simulation from AUT equivalent currents model and UASAM measurements.

fields) are recovered on a 70 cm × 70 cm plane placed in front of the AUT aperture. For comparison purposes, equivalent magnetic currents using simulated NF at the UAV flight path positions are also recovered. The inverse problem to be solved involves 22500 equations (NF samples at the two measurement domains) and 225 unknowns. Thanks to the use of the GPU version of the pSRM [33], equivalent currents are recovered in less than 10 s.

Reconstructed equivalent currents are depicted in Fig. 16, showing that the placement of the two horn antennas as well as the relative emitted power level of each of them can be identified. As expected, in the case of UASAM, measurements uncertainties (geo-referring errors, AUT-probe in-flight misalignments) degrade the quality of the reconstruction. It must be pointed out that the use of amplitude-only information also impacts the results, as it can be noticed when comparing Fig. 16 (a) and Fig. 16 (b).

From the aperture fields, the AUT radiation pattern can be calculated. Taking into account the height of the

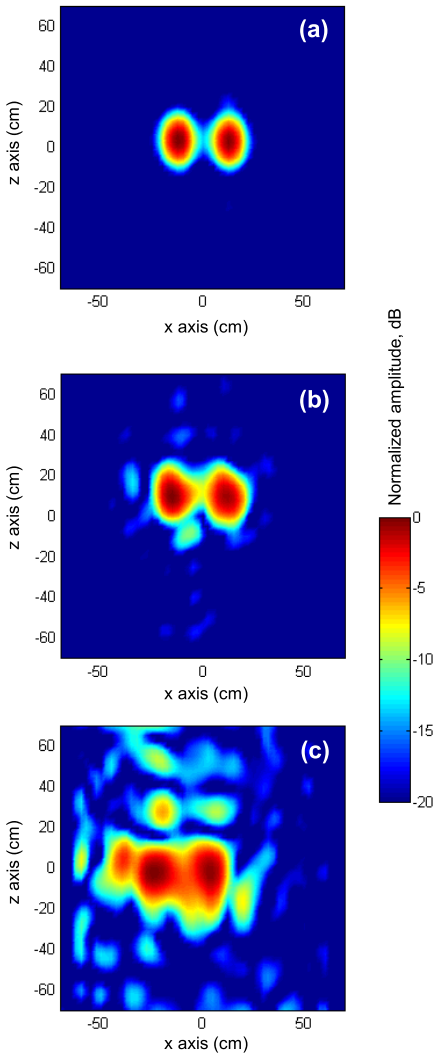

FIGURE 16. Reconstructed aperture fields (equivalent magnetic currents), $f = 2950$ MHz. (a) From simulated NF at UAV positions, considering amplitude and phase information. (b) From simulated NF at UAV positions, phaseless reconstruction. (c) From measured NF amplitude.

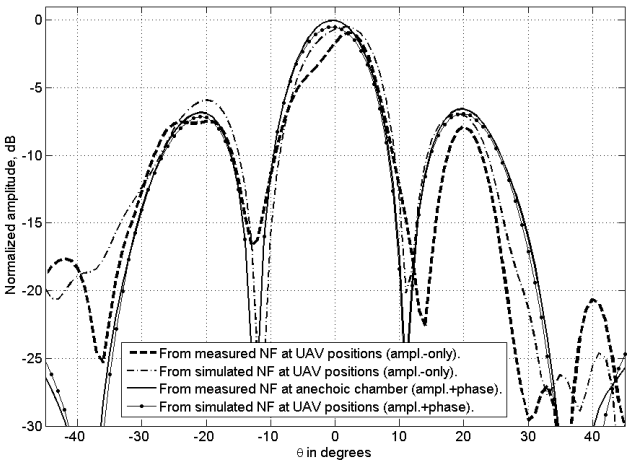

FIGURE 17. AUT far field pattern comparison (H plane). $f = 2950$ MHz.

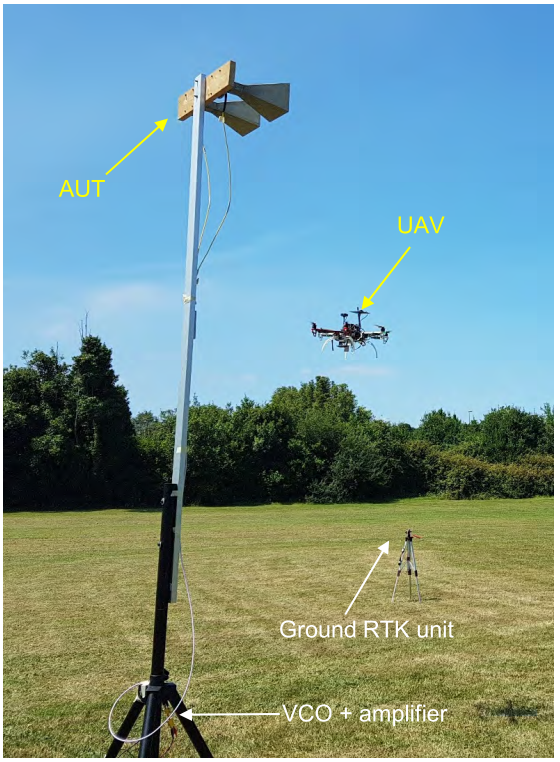

FIGURE 18. Picture of the UASAM measurement setup. AUT: array of two horn antennas at 4650 MHz.

cylinder (2 m, from 2 m to 4 m) and the radius (4.5 m) of the outer cylinder, the valid angular margin in the vertical plane (E plane) is just 25° [32]. In the horizontal plane (H plane), no truncation errors occur. FF pattern comparison is depicted in Fig. 17. As in the case of aperture fields, geo-referring errors and AUT-probe in-flight misalignments are the main sources of error that results in 4-5 dB discrepancies between FF pattern from NF measurements at spherical range in anechoic chamber, and FF pattern from NF measurements using the UASAM. These differences are in agreement with the ones depicted in Fig. 10, where the impact of geo-referring errors was analyzed.

B. C-BAND HORN ANTENNA ARRAY

In this example, the S-band horn antennas of Section V.A have been replaced by two horn antennas working at 4 – 6 GHz. Measurements were conducted at 4650 MHz using the commercial printed monopole antenna as probe. The AUT is fed with a Voltage Controller Oscillator (VCO) plus a RF amplifier that delivers up to +10 dBm. As in the previous example, the AUT is placed on top of a 3 m height pole (see Fig. 18). The two horn antennas are separated also 26 cm, but as the wavelength is smaller, the electrical distance is 4 λ, expecting more lobes in the radiation pattern. Given the AUT size, $D = 0.5$ m, FF distance is $R_{FF} = 7.8$ m.

For this example, two cylindrical grids at $R = 3$ m and $R = 4$ m have been considered, extending the height of the cylinders from 1.5 m to 4.5 m. Amplitude of the measured

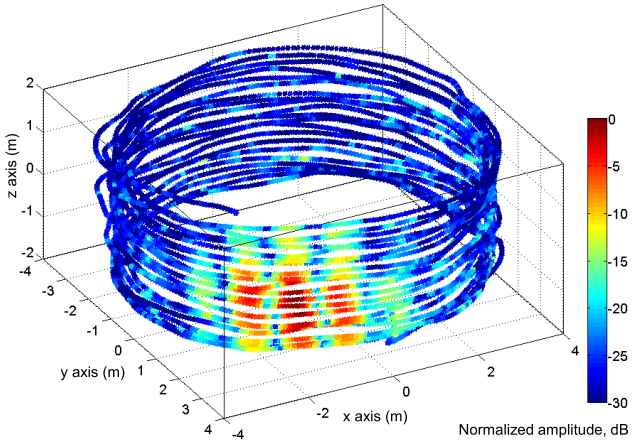

FIGURE 19. Measured amplitude of the NF radiated by the AUT at the UAV flight path positions. Targeted flight path: cylindrical domain of radius $R = 4$ m. $f = 4650$ MHz. Axes centered at the AUT position.

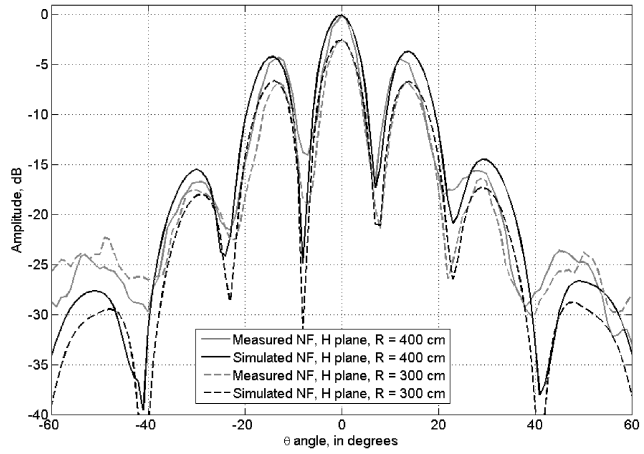

FIGURE 20. NF amplitude, H plane. $f = 4650$ MHz. Comparison between simulation from AUT equivalent currents model and UASAM measurements.

NF at the geo-referred UAV positions for the $R = 4$ m grid is plotted in Fig. 19. The presence of several sidelobes can be observed.

For validation purposes, the methodology depicted in Fig. 11 flowchart has been followed. Thus, a comparison between the measured NF and the NF radiated by an equivalent currents model of the AUT is plotted in Fig. 20. With respect to Example V.A (Fig. 15) it can be noticed a better agreement between simulated and measured NF. This is due to: i) the fact that the commercial printed probe antenna has a more symmetric pattern that the customized hexagon-shaped printed monopole antenna (see Section III), ii) UAV had a more stable flight (weaker wind gusts).

Next, the pSRM is applied to recover the equivalent magnetic currents on the AUT aperture plane (100 × 60 cm, discretized in 714 points). For this example, the number of NF field samples is around 19200. As in the Example of subsection V.A, the placement of the two horn antennas

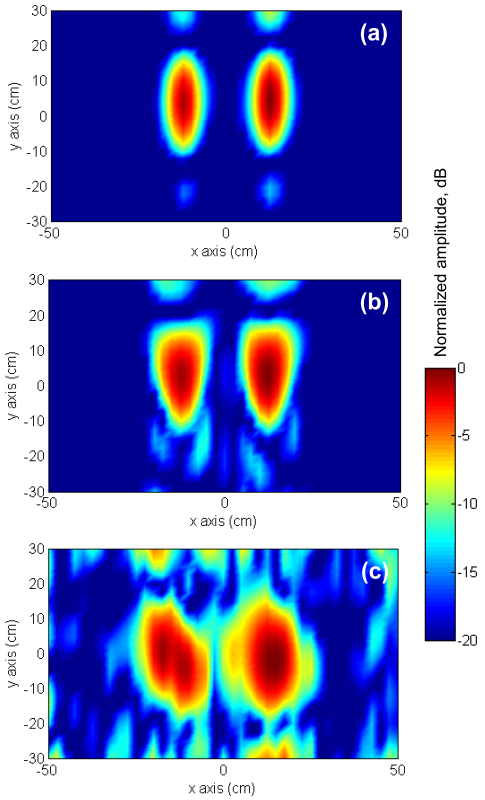

FIGURE 21. Reconstructed aperture fields (equivalent magnetic currents), $f = 4650$ MHz. (a) From simulated NF at UAV positions, considering amplitude and phase information. (b) From simulated NF at UAV positions, phaseless reconstruction. (c) From measured NF amplitude.

as well as the relative emitted power level of each can be identified (Fig. 21).

Finally, FF pattern is calculated from the reconstructed equivalent magnetic currents on the AUT aperture plane. Results depicted in Fig. 22 show 4-5 dB difference between FF patterns calculated from simulated NF at UAV positions and from amplitude-only measurements. Again, the error level is in agreement with the one observed in Fig. 10, for a geo-referring error of $\sigma_{x,y} = 2$ cm, $\sigma_z = 1$ cm.

VI. DISCUSSION

Table 1 compares the technical specifications of the presented UASAM with other UAV-based antenna measurement systems described in Section I. Concerning the question about which system provides better performance, the answer is that it depends on the application. For example, [15] is suitable for accurate antenna measurement up to 40 GHz where the cost and complexity of the system does not matter. For fast, simple evaluation of far field patterns, either [10], [11] or UASAM provide similar performance. UASAM distinctive feature is the capability of working in the NF region and performing antenna diagnostics.

It must be remarked that smaller, low-weight UAVs provide safer operating conditions when flying in the vicinity of the AUT, as in the case of NF measurements. The use of small

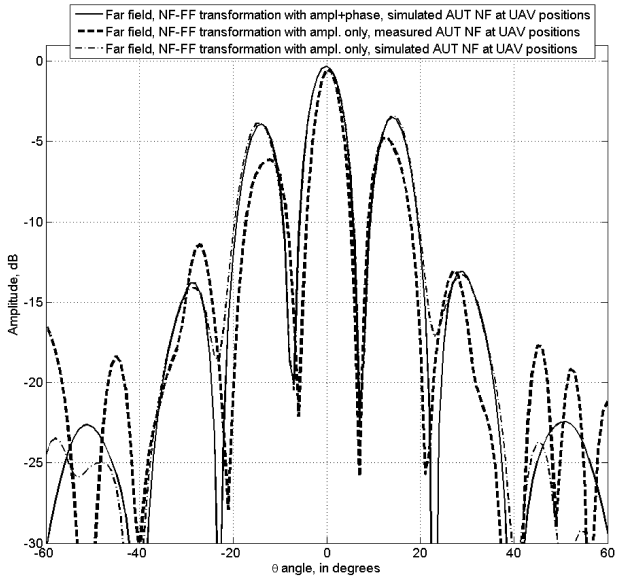

FIGURE 22. AUT far field pattern comparison (H plane). $f = 4650$ MHz.

TABLE 1. Comparison of UAV-based antenna measurement systems.

	[10]	[11]	[15]	UASAM
Frequency range	9 kHz – 12 GHz	30 – 900 MHz	Up to C band (8 GHz)	4 – 8 GHz
Positioning system accuracy	GPS. Angular resol. 1º	GPS / DGPS. Up to 1 cm with a tracking station.	Laser-tracker (less than 1 mm)	RTK and laser altimeter (1-2 cm)
EM field sensor / device	Spectrum analyzer	RF signal generator	Coherent detector	Power sensor
Antenna onboard the UAV	Wideband / omni-directional antennas	Dipole antenna	Standard Gain Horn [14].	Printed monopole
Maximum power level	+10 dBm	+8 dBm	Not specified	+5 dBm
Autonomous flight	25 min	15 min	Wired from a ground power supply	25 min
Estimated cost [a]	Not specified	< 2500 EUR	Not specified	< 1500 EUR
Measure-ment region	Far field	Far field	Near field and Far field	Near field and Far field
Radiation pattern uncertainty	+/- 3 dB	1 dB	Less than 1 dB	+/- 4 dB

[a] Ground Station (laptop) not included in the estimated cost.

UAVs minimizes the risk of damaging the AUT in case of an accidental collision. Even when flying hundreds of meters away from the antenna for direct FF measurements, piloting larger RPAs requires higher degree of expertise. Furthermore, practical limitations of FF measurements due to flight restrictions should be taken into account.

Besides, civil regulations and required licenses for UAV operation in non-controlled airspace are related to UAV take-off weight [36]: heavier UAVs require additional license degree and are subject to more restrictive regulations (e.g. regarding beyond line of sight operation), which eventually impacts on the overall operation cost.

VII. CONCLUSION

Results presented in this contribution prove the feasibility of the UASAM for antenna diagnostics and characterization. The combination of a cm-level accurate geo-referring system and an algorithm capable of handling NF amplitude-only measurements taken at arbitrary-geometry acquisition domains have contributed to simplify the hardware and sensors required onboard the UAV, resulting in a compact, low-cost, and accurate antenna measurement system. Quick deployment time and ease-of-operation make UASAM of interest for rapid in-situ antenna testing of a wide variety of wireless communications systems such as radio and television broadcasting, mobile networks, radionavigation systems.

ACKNOWLEDGEMENT

This work has been developed under the framework of the Universidad de Oviedo degree Expert in Remotely Piloted and Autonomous Flight Aircrafts (www.dronesuniovi.es). A. Arboleya was with the Área de Teoría de la Señal y Comunicaciones, Universidad de Oviedo, Gijón, Spain.

REFERENCES

[1] A. C. Satici, H. Poonawala, and M. W. Spong, "Robust optimal control of quadrotor UAVs," *IEEE Access*, vol. 1, pp. 79–93, 2013.
[2] N. Gageik, P. Benz, and S. Montenegro, "Obstacle detection and collision avoidance for a UAV with complementary low-cost sensors," *IEEE Access*, vol. 3, pp. 599–609, 2015.
[3] P. Jacob, R. P. Sirigina, A. S. Madhukumar, and V. A. Prasad, "Cognitive radio for aeronautical communications: A survey," *IEEE Access*, vol. 4, pp. 3417–3443, 2016.
[4] S. Campana, "Drones in archaeology. State-of-the-art and future perspectives," *Archaeol. Prospect.*, vol. 9999, pp. 1–22, Feb. 2017, doi: 10.1002/arp.1569.
[5] A. Capolupo, S. Pindozzi, C. Okello, N. Fiorentino, and L. Boccia, "Photogrammetry for environmental monitoring: The use of drones and hydrological models for detection of soil contaminated by copper," *Sci. Total Environ.*, vol. 514, pp. 298–306, May 2015.
[6] P. Liu *et al.*, "A review of rotorcraft unmanned aerial vehicle (UAV) developments and applications in civil engineering," *Smart Struct. Syst.*, vol. 13, no. 6, pp. 1065–1094, 2014.
[7] M. Erdelj, E. Natalizio, K. R. Chowdhury, and I. F. Akyildiz, "Help from the sky: Leveraging UAVs for disaster management," *IEEE Pervasive Comput.*, vol. 16, no. 1, pp. 24–32, Jan./Mar. 2017.
[8] E. Teng, J. D. Falcao, C. R. Dominguez, F. Mokaya, P. Zhang, and B. Iannucci, "Aerial sensing and characterization of three-dimensional RF fields," in *Proc. 2nd Int. Workshop Robot. Sensor Netw.*, Seattle, WA, USA, Apr. 2015, pp. 1–6.
[9] J. Kean, "Measurement of broadcast antennas takes off," *Radioworld Newslett.*, Mar. 2017. Accessed: Aug. 11, 2017. [Online]. Available: http://www.radioworld.com/nab-show/0028/measurement-of-broadcast-antennas-takes-off/339417
[10] J. Schreiber, "Antenna pattern reconstitution using unmanned aerial vehicles (UAVs)," in *Proc. IEEE Conf. Antenna Meas. Appl. (CAMA)*, Syracuse, NY, USA, Oct. 2016, pp. 1–3.
[11] G. Virone *et al.*, "Antenna pattern verification system based on a micro unmanned aerial vehicle (UAV)," *IEEE Antennas Wireless Propag. Lett.*, vol. 13, pp. 169–172, 2014.
[12] F. Paonessa *et al.*, "UAV-based pattern measurement of the SKALA," in *Proc. IEEE Int. Symp. Antennas Propag., USNC/URSI Nat. Radio Sci. Meet. (APSURSI)*, Vancouver, BC, Canada, Jul. 2015, pp. 1372–1373.

[13] T. Schrader, J. Bredemeyer, M. Mihalachi, J. Rohde, and T. Kleine-Ostmann, "Concept and design of a UAS-based platform for measurements of RF signal-in-space," *Adv. Radio Sci.*, vol. 14, pp. 1–9, Sep. 2016, doi: 10.5194/ars-14-1-2016.
[14] T. Fritzel *et al.*, "Advances in the development of an airborne near-field test facility (ANTF)," in *Proc. 24th AMTA Eur.*, Munich, Germany, May 2006, pp. 1–7.
[15] T. Fritzel, R. Strauss, H.-J. Steiner, C. Eisner, and T. Eibert, "Introduction into an UAV-based Near-Field system for in-situ and large-scale antenna measurements," in *Proc. IEEE Conf. Antenna Meas. Appl. (CAMA)*, Syracuse, NY, USA, Oct. 2016, pp. 1–3, doi: 10.1109/CAMA.2016.7815762.
[16] F. Paonessa, G. Virone, P. Bolli, and A. M. Lingua, "UAV-based antenna measurements: Scan strategies," in *Proc. 11th Eur. Conf. Antennas Propag. (EUCAP)*, Paris, France, Mar. 2017, pp. 1303–1305.
[17] Y. Á. López, C. Cappellin, F. Las-Heras, and O. Breinbjerg, "On the comparison of the spherical wave expansion-to-plane wave expansion and the sources reconstruction method for antenna diagnostics," *Prog. Electromagn. Res.*, vol. 87, pp. 245–262, Nov. 2008.
[18] T. F. Eibert and C. H. Schmidt, "Multilevel fast multipole accelerated inverse equivalent current method employing Rao–Wilton–Glisson discretization of electric and magnetic surface currents," *IEEE Trans. Antennas Propag.*, vol. 57, no. 4, pp. 1178–1185, Apr. 2009.
[19] Y. Álvarez, F. Las-Heras, and C. García, "The sources reconstruction method for antenna diagnostics and imaging applications," *Solutions and Applications of Scattering, Propagation, Radiation and Emission of Electromagnetic Waves*, A. Kishk, Ed. Rijeka, Croatia: InTech, 2012, doi: 10.5772/50744.
[20] J. L. A. Quijano, L. Scialacqua, J. Zackrisson, L. J. Foged, M. Sabbadini, and G. Vecchi, "Suppression of undesired radiated fields based on equivalent currents reconstruction from measured data," *IEEE Antennas Wireless Propag. Lett.*, vol. 10, pp. 314–317, 2011.
[21] S. F. Razavi and Y. Rahmat-Samii, "A new look at phaseless planar near-field measurements: Limitations, simulations, measurements, and a hybrid solution," *IEEE Antennas Propag. Mag.*, vol. 49, no. 2, pp. 170–178, Apr. 2007.
[22] Y. Álvarez, F. Las-Heras, and M. R. Pino, "The sources reconstruction method for amplitude-only field measurements," *IEEE Trans. Antennas Propag.*, vol. 58, no. 8, pp. 2776–2781, Aug. 2010.
[23] J. L. Martínez, A. Arboleya-Arboleya, Y. Álvarez-López, C. García-González, and F. Las-Heras, "Phaseless antenna diagnostics based on off-axis holography with synthetic reference wave," *IEEE Antennas Wireless Propag. Lett.*, vol. 13, pp. 43–46, 2014.
[24] A. El-Rabbany, *Introduction to GPS: The Global Positioning System*. London, U.K.: Artech House, 2002.
[25] DJI. *Frame Wheel ARF Kit*. Accessed: Jul. 12, 2017. [Online] Available: https://www.dji.com/es/flame-wheel-arf/feature
[26] *NAVIO2—Emlid*. Accessed: Jul. 12, 2017. [Online] Available: https://emlid.com/navio/
[27] *Raspberry Pi*. Accessed: Jul. 14, 2017. [Online] Available: https://www.raspberrypi.org/products/
[28] *AD8318 1 MHz-to-8 GHz Logarithmic Detector and Controller From Analog Devices*. Accessed: Jul. 12, 2017. [Online] Available: http://www.analog.com/en/products/rf-microwave/rf-power-detectors/non-rms-responding-detector/ad8318.html#product-overview
[29] *NEO-LEA M8T Chip From U-Blox*. Accessed: Jul. 12, 2017. [Online] Available: https://www.u-blox.com/en/product/neolea-m8t-series
[30] *SF10/A Laser Altimeter From LightWare Optoelectronics*. Accessed: Jul. 12, 2017. [Online] Available: http://lightware.co.za/shop2017/drone-altimeters/26-sf10a-25-m.html
[31] C. Balanis, *Advanced Engineering Electromagnetics*. New York, NY, USA: Wiley, 1989.
[32] A. Yaghjian, "An overview of near-field antenna measurements," *IEEE Trans. Antennas Propag.*, vol. 56, no. 1, pp. 30–45, Jan. 1986.
[33] J. C. F. González, M. L. Portugués, Y. Á. López, J. A. López-Fernández, and F. L.-H. Andrés , "GPU-based computational acceleration of phaseless algorithms for antenna characterization," in *Proc. 11th Eur. Conf. Antennas Propag. (EUCAP)*, Paris, France, Mar. 2017, pp. 1452–1456.
[34] *Broadspec UWB Antenna From TimeDomain*. Accessed: Jul. 13, 2017. [Online]. Available: http://www.timedomain.com/datasheets/TD_Broadspec_Antenna.pdf
[35] S. Singhal and A. K. Singh, "CPW-fed hexagonal Sierpinski super wideband fractal antenna," *IET Microw., Antennas Propag.*, vol. 10, no. 15, pp. 1701–1707, 2016.
[36] *Spanish Aviation Safety and Security Agency AESA, RPA/UAV Regulation*. Accessed: Jun. 10, 2016. [Online]. Available: http://www.seguridadaerea.gob.es/LANG_EN/cias_empresas/trabajos/rpas/default.aspx

MARÍA GARCÍA-FERNÁNDEZ (S'15) was born in Luarca, Spain, in 1992. She received the M.Sc. degree in telecommunication engineering from the University of Oviedo, Gijón, Spain, in 2016, where she is currently pursuing the Ph.D. degree. She was a Visiting Student with Stanford University, Stanford, CA, USA, in 2013 and 2014. Since 2013, she has been involved in several research projects within the Area of Signal Theory and Communications, University of Oviedo. Her current research interests include inverse scattering, remote sensing, radar, and imaging techniques.

Yuri Álvarez López (S'06–M'09–SM'15) was born in Langreo, Spain, in 1983. He received the M.S. and Ph.D. degrees in telecommunication engineering from the University of Oviedo, Gijón, Spain, in 2006 and 2009, respectively. He was a Visiting Scholar with the Department of Electrical Engineering and Computer Science, Syracuse University, Syracuse, NY, USA, in 2006 and 2008; and held a visiting post-doctoral position at the Gordon Center for Subsurface Sensing and Imaging Systems and the Awareness and Localization of Explosive Related Threats Center of Excellence, Northeastern University, Boston, MA, USA, from 2011 to 2014; and held a visiting post-doctoral position at the ELEDIA Research Center, Trento, Italy, in 2015. He is currently an Assistant Professor with the Signal Theory and Communications, University of Oviedo, Gijón, Spain. His research interests include antenna diagnostics, antenna measurement techniques, RF techniques for indoor location, inverse scattering and imaging techniques, and phaseless methods for antenna diagnostics and imaging. Prof. Lopez was a recipient of the 2011 Regional and National Awards to the Best Ph.D. Thesis on Telecommunication Engineering (category: security and defense).

ANA ARBOLEYA received the M.Sc. degree in telecommunication engineering and the Ph.D. degree in telecommunication engineering from the University of Oviedo, Spain, in 2009 and 2016, respectively. From 2008 to 2016, she was as a Research Assistant within the Signal Theory and Communications Research Group, TSC-UNIOVI, at the Department of Electrical Engineering, University of Oviedo. She was a Visiting Scholar in 2014 and 2015 in the Department of Radio Science and Engineering and MilliLab, in Aalto University, Finland. She holds a post-doctoral position at the EpOC Polytech' Laboratory (Electronics for Connected Objects), University of Nice-Sophia Antipolis, France. Her major research interests comprise antenna diagnostics and measurement systems and techniques, and high-frequency imaging techniques and applications. Dr. Arboleya was a recipient of the 2017 National Awards of the Official College of Telecommunication Engineers of Spain to the Best Ph.D. Thesis on Telecommunication Engineering in the category of security and defense.

BORJA GONZÁLEZ-VALDÉS (S'09–M'12) received the B.S and Ph.D. degrees in electrical engineering from the University of Vigo, Vigo, Spain, in 2006 and 2010, respectively. From 2006 to 2010, he was with the Antenna and Optical Communications Group, University of Vigo. From 2008 to 2009, he was a Visiting Researcher with the Gordon Center for Subsurface Sensing and Imaging Systems, Northeastern University, Boston, MA, USA. In 2011, he joined the Awareness and Localization of Explosives-Related Threats Center of Excellence, Northeastern University. Since 2015, he has been a Post-Doctoral Researcher with the AtlantTIC Research Center, University of Vigo. His research interests include antenna design, inverse scattering, radar, advanced imaging techniques, and terahertz technology.

YOLANDA RODRIGUEZ-VAQUEIRO (S'12) received the B.S. and M.S. degrees in electrical engineering from the University of Vigo, Vigo, Spain, in 2009, and the Ph.D. degree in electrical engineering from Northeastern University, Boston, MA, USA, in 2015. Her Ph.D. thesis was Compressive Sensing for Electromagnetic Imaging Using a Nesterov-Based Algorithm. She is currently a Post-Doctoral Researcher with the AtlantTIC Research Center, University of Vigo. In 2011, she received a Research Assistant grant from the Awareness and Localization of Explosive Related Threats Center of Excellence, Northeastern University. She was also granted as a Junior Researcher with the University of Vigo. Dr. Rodriguez-Vaqueiro was a recipient of the Research-Impact Award from the Department of Electrical and Computer Engineering, Northeastern University (for her work during the Ph.D. studies), the Best Paper Award in the 2012 IEEE Homeland Security Conference, Honorable Mention in the Student Paper Competition in the 2013 IEEE APS/URSI Conference, the Best Paper Award in the 2014 European Conference on Antennas and Propagation, the Burke/Yannas Award to the most original research study in the field of bioengineering in the 2015 American Burn Association Meeting, and the Research-Impact Award from the Department of Electrical and Computer Engineering, Northeastern University, in 2015.

MARÍA ELENA DE COS GÓMEZ received the M.S. and Ph.D. degrees from the Universidad de Cantabria, in 2002 and 2006, respectively. She was involved in nonlinear dynamics: stability and phase-noise analysis of nonlinear circuits, such as oscillators, frequency dividers, self-oscillating mixers, and multiharmonic generators. She was a Researcher Engineer in collaboration with ACORDE S.A from 2004 to 2007. She joined TSC-UNIOVI in 2007. She was an Invited Professor with the I.E.T.R. Rennes, France, in 2011 and 2014, respectively. She was an Associate Editor of the *International Journal of Antennas and Propagation*. Her research interests are metamaterials design and its applications to antennas and microwave circuits, design of antennas for RFID systems, location techniques, and wireless sensor networks design and applications.

FERNANDO LAS-HERAS ANDRÉS (M'86–SM'08) received the M.S. and Ph.D. degrees in telecommunication engineering from the Technical University of Madrid (UPM), in 1987 and 1990, respectively. He was a National Graduate Research Fellow from 1988 to 1990 and he was an Associate Professor with the Department of Signal, Systems and Radiocommunications, UPM, from 1991 to 2000. He was a Visiting Lecturer with the National University of Engineering, Peru, in 1996, a Visiting Researcher with Syracuse University, New York, in 2000, and a short-term Visiting Lecturer with ESIGELEC, France, from 2005 to 2011. He held the Telefónica Chair on RF Technologies, ICTs applied to Environment, and ICTs and Smartcities at the University of Oviedo from 2005 to 2015. Since 2003, he has been a Full Professor with the University of Oviedo, where he was the Vice-Dean for telecommunication engineering with the Technical School of Engineering at Gijón from 2004 to 2008. Since 2001, he has been Head of the research group Signal Theory and Communications TSC-UNIOVI at the Department of Electrical Engineering, University of Oviedo. He has authored over 300 articles published in academic journals and proceedings of international conferences, mainly in the areas of antenna design and the inverse electromagnetic problem with applications in diagnostic, measurement and synthesis of antennas, metasurfaces, phaseless techniques, propagation, and microwave to terahertz imaging and localization, as well as in engineering education. He was a member of the board of directors of the IEEE Spain Section from 2012 to 2015. Since 2010, he has been a member of the Science, Technology and Innovation Council of Asturias.